OMAE2011-49924

SPACE-TIME WAVES AND SPECTRA IN THE NORTHERN ADRIATIC SEA VIA A WAVE ACQUISITION STEREO SYSTEM

Francesco Fedele
School of Civil and Environmental Engineering
Georgia Institute of Technology, Savannah, USA

Alvise Benetazzo
PROTECNO Srl,
Noventa Padovana, Italy

George Z. Forristall
Forristall Ocean Eng., Inc.
Maine, USA

ABSTRACT

A novel Wave Acquisition Stereo System (**WASS**) is proposed for the stereo reconstruction of oceanic waves both in space and time. To test the performance of such video observational technology, we have deployed **WASS** at the oceanographic tower *Acqua Alta* in the Northern Adriatic Sea, off the Venice coast in Italy. The analysis of WASS video measurements yielded accurate estimates of the oceanic sea state dynamics, the associated directional spectra and wave surface statistics that agree well with theoretical models. Further, the expected largest wave surface height over an area is estimated via both Piterbarg's theory (Piterbarg 1995) and Adler's Euler characteristics (Adler 1981, Adler and Taylor 2007). It is found that the largest surface height over the imaged area is considerably larger than the maximum crest observed in time at a single point, in agreement with theoretical predictions.

INTRODUCTION

The prediction of large waves is typically based on the statistical analysis of time series of the wave surface displacement retrieved from wave gauges, ultrasonic instruments or buoys at a fixed point P of the ocean. However, in short-crested seas the surface time series gathered at the given location tends to underestimate the true actual wave surface maximum that can occur over a given region of area E_s around P. Indeed, large waves travel on top of wave groups, and the probability that the group passes at its apex through P is practically null. The large crest height recorded in time at P is simply due to the dynamical effects of a wave group that focuses nearby that location within or outside E_s forming a larger wave crest. Thus, point measurements can underestimate the maximum wave group surface height η_{max} attained over E_s, which is not necessarily the highest crest height of the group, unless the area is large enough to embed the entire group dynamics. Indeed, η_{max} can also occur on the region's boundaries, and this is usually the case for smaller areas than the wave group's size. Only in narrow-band sea states, point measurements are exact in predicting such maximum which is expected to be the same at any point in space. However, realistic oceanic conditions are generally short-crested and the expected η_{max} can be underestimated if wave extremes are not modeled both in space and time as maxima of random fields rather than those of random processes of time (Adler 1981, Piterbarg 1995, Adler and Taylor 2007). Quantifying such underestimation is of relevant significance in offshore industry for a proper design of the air gap under the deck of fixed offshore structures. Indeed, localized damages have sometimes been observed on the lower decks of platforms after storms.

This may be due to a design that is based on the expected largest crest height from point measurements that underestimate the expected global maximum, i.e. the largest wave surface height, over the rig's area footprint. This can be predicted via applications of Piterbarg's results on global maxima of Gaussian fields (Piterbarg 1995), or by the Euler characteristics of excursion sets (Adler 1981, Adler and Taylor 2007). Forristall (2006) applied for the first time Piterbarg's theorem to the air gap problem showing that it can explain observed damages during hurricanes (Forristall 2007).

The application of such advanced stochastic theories to realistic oceanic conditions requires the availability of wave surface data measurements collected in space on the scale of few hundred meters or smaller. At such scales, the main difficulty for such measurements is that radar or SAR remote sensing is not accurate enough to reconstruct the space-time dynamics and associated spectral properties. On the other hand, a two dimensional wave probe-type array could be used but it can be expensive to install and maintain. A low-cost alternative is a novel non-intrusive optical sensor, the so-called Wave Acquisition Stereo System (**WASS**) (Benetazzo 2006). **WASS** exploits the state-of-the-art epipolar methods in computer vision (Ma et al. 2004, Benetazzo 2006) for the 3-D stereo reconstruction of both the spatial and temporal dynamics of ocean waves. It has a significant advantage as a low-cost system in both installation and maintenance (Holland et al. 1997, Holland & Holman 1997). A stereo camera view provides both spatial and temporal data whose statistical content is richer than that of a time series retrieved from wave gauges (Benetazzo 2006). For example, Shemdin et al. (1988) and Banner et al. (1989) proposed the directional measurements of short ocean waves applying stereography. In particular, Banner et al. (1989) applied stereographic measurements in order to study wavenumber spectra of short gravity waves. A quite recent integration of stereographic techniques in oceanography was the WAVESCAN project (Santel et al., 2004) which contributed to the important extension of the analysis of stereographic pairs in time. Further, Wanek and Wu (2006) proposed a trinocular stereo system for ocean wave detection.

In this paper, we present results from the analysis of **WASS** measurements acquired during several experimental campaigns at the oceanographic tower *Acqua Alta* in the Northern Adriatic Sea (see Figure 1). In particular, we first describe the deployment of **WASS** at *Acqua Alta*, and then discuss the estimates of the spectral properties of the observed oceanic sea state dynamics, as well as wave surface statistics. Finally, estimates of the expected largest wave surface height over an area are compared against both Piterbarg's theory (Piterbarg 1995) and Adler's Euler characteristics (Adler 1981, Adler and Taylor 2007).

Figure 1: "Acqua Alta" tower off the Venice beach, Italy.

WASS DEPLOYMENT AT 'ACQUA ALTA'

The '*Acqua Alta*' tower of the CNR-ISMAR Institute is located in the Northern Adriatic Sea, East of Italy, 16 km off the coastline of Venice, on 16 m depth. The tower was used as the calibration site for the ERS-1 radar altimeter.

The tower was built in 1970. As one can see from Figure 1, its basic structure is a four-leg-framed template extending 4 m above the sea surface. The template is firmly fixed on the bottom, the poles penetrating 22 m inside the sediments. The housing structure (three floors plus the top terrace) is firmly joined to the upper end of the template. The submerged part is protected by zinc anodes. The splash zone (+3, -2 m) is covered with a fully protective layer of epoxy resin. The three floors are at 4.5, 6.7, 9.3 m above the mean sea level, respectively. The terrace floor is at 12.3 m. The tower is equipped with 380, 220, 125 VAC 50 Hz, available when personnel are on board. A large set of batteries provides 12 and 24 VDC for occasional measurements and for some basic regular needs. The tower is also equipped with a meteo-oceanographic station. The data are recorded on board and also sent to land by telemeters. The station includes measurements of wind, temperature, humidity, solar radiation, rain, waves (directional), tides and sea temperature. The water level has been recorded since 1971. Two tide gauges of the conventional well type are installed. Wave gauges are also operational and consist of three pressure transducers located on three of the four platform legs at 5 m depth. Continuous recording is performed for 17 min every 3 h. The system, which allows an estimate of the directional wave spectrum, has, with appropriate upgrading, been operational since 1978.

Figure 2: (Left) deployed WASS at *Acqua Alta*, and (Right) workstation and cables.

We have deployed **WASS** on the North-East side of the tower in order to have a camera field of view with respect to both the Scirocco and Bora wind sea states (see left panel of Figure 2). Further, **WASS** has been installed at the third floor of the tower to maximize the stereo camera field view. **WASS** allows acquiring synchronized images from the two cameras and stored in the hard drive of a workstation (see right panel of Figure 3). Such stereo system must be calibrated. To do so, standard image analysis techniques (Ma et al. 2004) exploit a given known reference (for example, a chess-board as shown in Figure 3 to estimate *internal parameters* such as i) lens focal length, ii) principal point, and distortion, i.e. lens angular aberration (see Figure 4) as well as *external parameters* which yield the reciprocal position of the two cameras with respect to a fixed reference world system. During the field campaign at *Acqua Alta*, five calibration sessions were completed (see Figure 3).
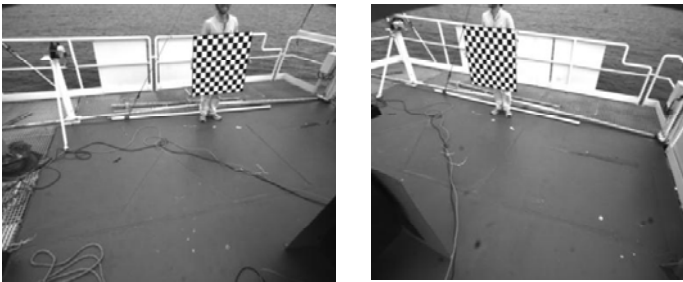

Figure 3: Left panel: example of left camera image used for stereo calibration. Right panel: example of right camera image used for stereo calibration.

WAVE MEASUREMENTS AT "ACQUA ALTA"

Video data were collected by **WASS** during three field campaigns at *Acqua Alta* in 2009-2010 (see Table 1). The three experiments cover a broad range of wave height conditions and steepness ε as shown in Table 2. Here, T_p is the peak wave period, ε is defined as the ratio between the significant wave height H_s and the average wavelength L_{mean} estimated from the

average zero-crossing period T_z via the linear dispersion (water depth d=16 m). Experiment 3, with a much higher wind speed, exhibited the largest H_s / L_{mean} ratio among the three wave fields and the acquired videos confirmed the occurrence of wide spread breaking. Figure 5 illustrates various images framed by the right camera and the associated reconstructed wave surface, also providing an idea of the wave conditions during Experiment 2.
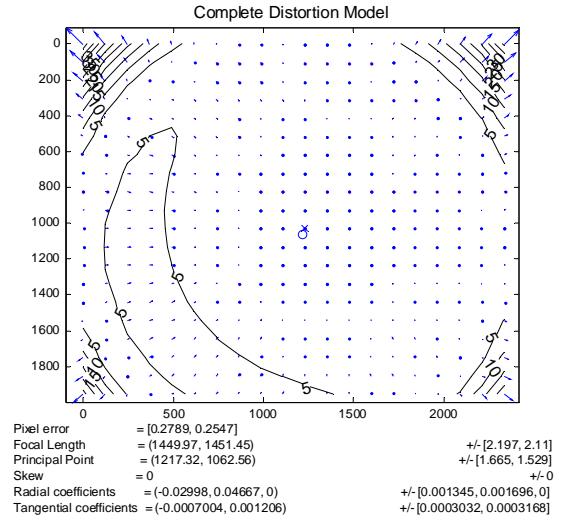

Pixel error   = [0.2789, 0.2547]
Focal Length   = (1449.97, 1451.45)   +/- [2.197, 2.11]
Principal Point   = (1217.32, 1062.56)   +/- [1.665, 1.529]
Skew   = 0   +/- 0
Radial coefficients   = (-0.02998, 0.04667, 0)   +/- [0.001345, 0.001696, 0]
Tangential coefficients = (-0.0007004, 0.001206)   +/- [0.0003032, 0.0003168]

Figure 4: Typical pixel error due to angular aberration of lens.

Table 1: Experiments at Acqua Alta

Exp #	Starting Date, hour	Wind Speed [m/s, dir from]	# frames/rate [-,fps]
1	2009/06/05, 1428 UTC	6.5, 133.0 (±11.3)°N	6000/10
2	2009/10/14, 0755 UTC	6.3, 90.0 (±11.3)°N	21000/10
3	2010/03/09, 1120 UTC	17.9, 67.5 (±11.3)°N	9000/5

Table 2: Wave conditions during the three experiments at *Acqua Alta* (see Table 1). H_s=Significant wave height, T_p=peak wave period, T_z=zero up-crossing period, L_{mean}=mean wave length and ε=steepness.

Exp #	Date	H_s [m]	T_p [s]	T_z [s]	L_{mean} [m]	ε
1	2009/06/05	0.46	4.34	3.09	14.9	0.03
2	2009/10/14	1.10	4.83	3.62	20.5	0.05
3	2010/03/09	2.16	6.36	4.85	36.5	0.06

Table 3: Experiment 2. Comparison of WASS/CNR measurements. Direction with respect to the geographical North.

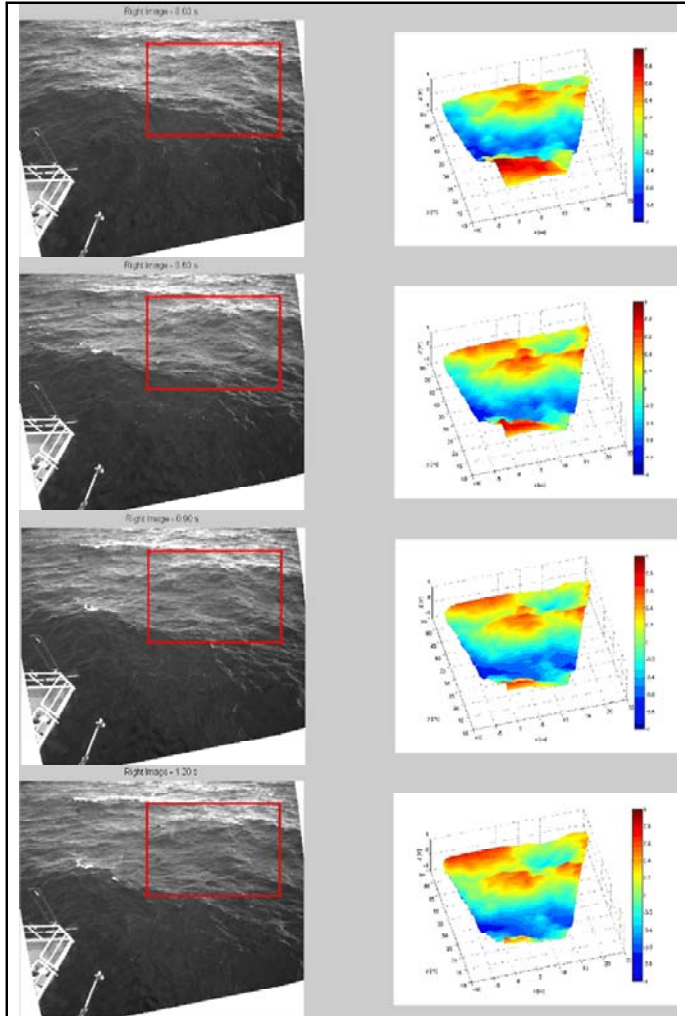|	$H_{1/3}$ [m]	H_{m0} [m]	$H_{1/10}$ [m]	T_p [s]	T_z [s]	H_{max} [m]	peak dir [deg]	mean dir [deg]
CNR	1.09	1.13	1.36	4.59	3.51	2.18	60.0±2	65.0±2
WASS	1.10	1.15	1.34	4.83	3.62	2.03	64.6±2	59.5±2

Figure 5: Experiment 2. Example of images framed by WASS (right camera) and correspondent stereo reconstructed wave surface (50 x50 m^2).
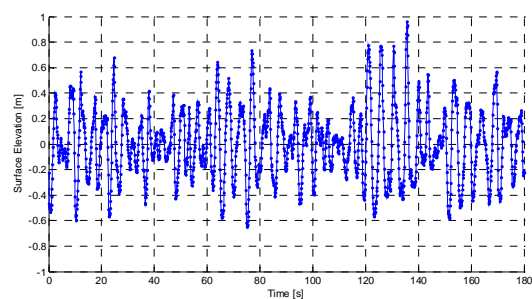

Figure 6: Experiment 2. Water elevation time series extracted from the stereo reconstructions of Figure 5.

WASS estimates were compared against reference point time series measurements provided by instruments available at *Acqua Alta* and managed by CNR-ISMAR. These are wired wave gauges and an AWAC ADCP. Such comparison was done by first selecting a virtual point probe within the reconstructed

area and then extracting the associated time series of the stereo reconstructed wave surface displacements (see Figure 6). Given the wave time series, various statistical and spectral properties of waves were computed and compared against those from *Acqua Alta* instruments, hereafter referred to as CNR measurements. As an example, Tables 3 reports such comparisons for experiment 2. Estimates of the significant wave heights H_{mo}, $H_{1/3}$ and $H_{1/10}$, and wave periods T_m and T_z follow from a zero-crossing analysis of the extracted time series low-pass filtered at roughly 1.0 Hz. The largest wave surface height estimated during the experiments is denoted with H_{max}. Such comparisons clearly prove that the accuracy of stereo measurements via **WASS** is comparable to that of more traditional wave instruments, and even when intense wave breaking occurs as that observed during Experiment 3 (see Figure 7). Even for these rough sea conditions, good agreement with CNR measurements is observed as shown in Table 4.
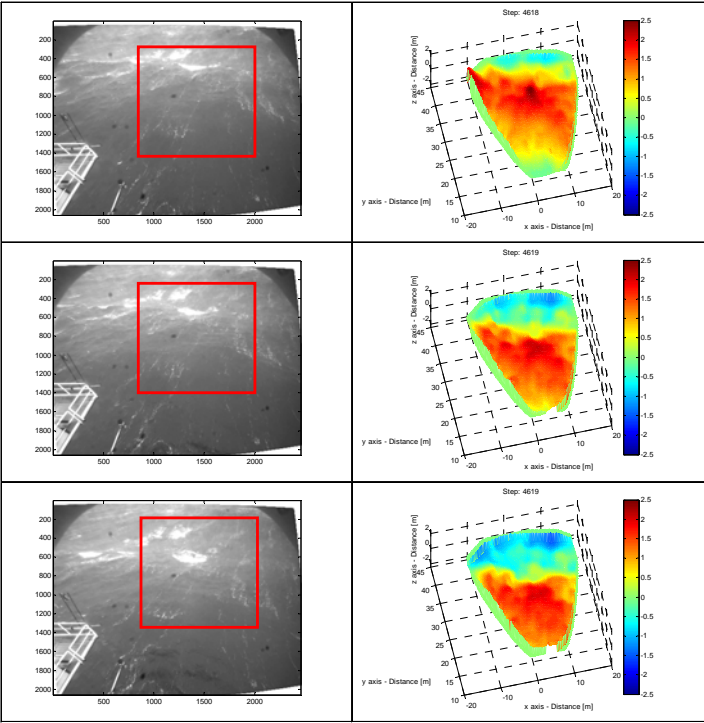

Figure 7: Experiment 3. Example of images framed by WASS (right camera) and correspondent stereo reconstructed wave surface.

Table 4: Experiment 3. Comparison of WASS/CNR measurements. Direction with respect to the geographical North.

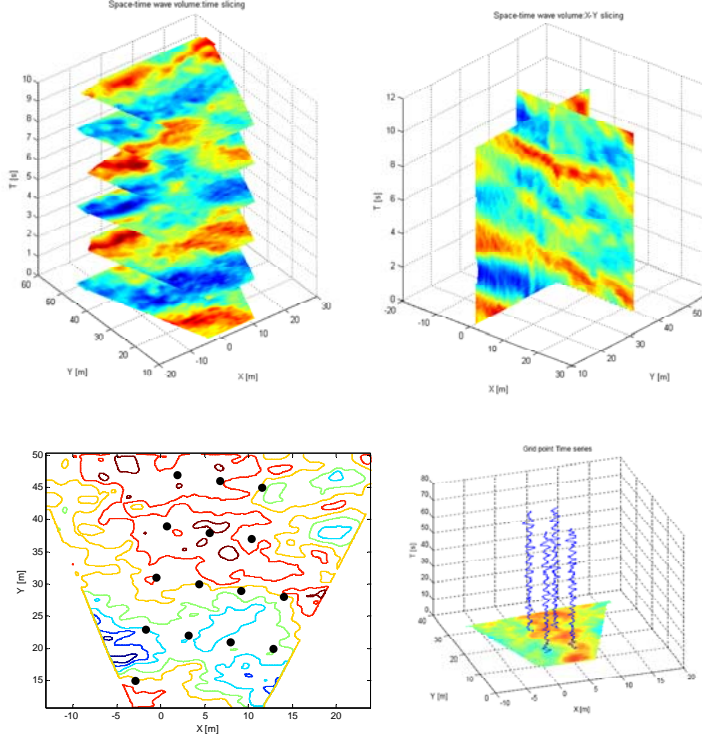|	$H_{1/3}$ [m]	H_{m0} [m]	$H_{1/10}$ [m]	T_p [s]	T_z [s]	H_{max} [m]	peak dir [deg]	mean dir [deg]
CNR	2.16	2.23	2.79	6.37	4.62	3.80	74.4±2	69.7±2
WASS	2.15	2.17	2.64	6.36	4.85	3.95	67.7±2	70.1±2

Figure 8: Experiment 2. (Top-left) horizontal slicing of the wave space-time volume V (sequence of snapshots); (Top-right) vertical slicing of V; (Bottom-left) location of the virtual probes and (Bottom-right) extracted time series.

WAVE SPECTRA

The four dimensional (4D) wave surface $z = \eta(x, y, t)$ stereo-reconstructed from the video images acquired by **WASS** during Experiment 2 defines a space-time volume V. Such 4D volume can be visualized via horizontal and vertical slicing as shown in Figure 8. In the same Figure, there are also plotted the time series of η extracted at several virtual point probles in the domain. Both wave spectra and statistics of waves are then computed by analyzing the ensemble of the extracted time series with a total number of roughly 7000 waves. The average significant wave height $H_s = 1.10$ m and the mean wave period T_m=3.62 s. Figure 9 shows the average frequency spectrum $S(f)$, mean of the observed spectra at all the virtual point probes. The Phillips' equilibrium range (Phillips, 1958) is not observed, but in agreement with Zakharov (1999) the spectrum tail decays as f^{-4}. We noticed noise above f_{max}=1.0 Hz, and thus ignored the energy content above it with variations less than 0.5% in the wave variance. Figure 10 shows the mean directional spectrum $S(k_x, k_y)$ obtained by averaging the 2D Fourier Transform of the 21000 3D reconstructed sea surface maps. Finally, in Figure 11 we compared the observed average

omni-directional spectrum $S(k)$ with that obtained from the average frequency spectrum of Figure 9 via the linear dispersion relation. The spectrum tail decays as $k^{-2.5}$ in agreement with Zakharov (1999). For experiment 3, the estimated frequency spectrum is shown in Figure 12. The associated saturation spectrum $S(f)f^n$ of Figure 13 clearly unveils an inertial range in agreement with Zakharov's theory (1999).
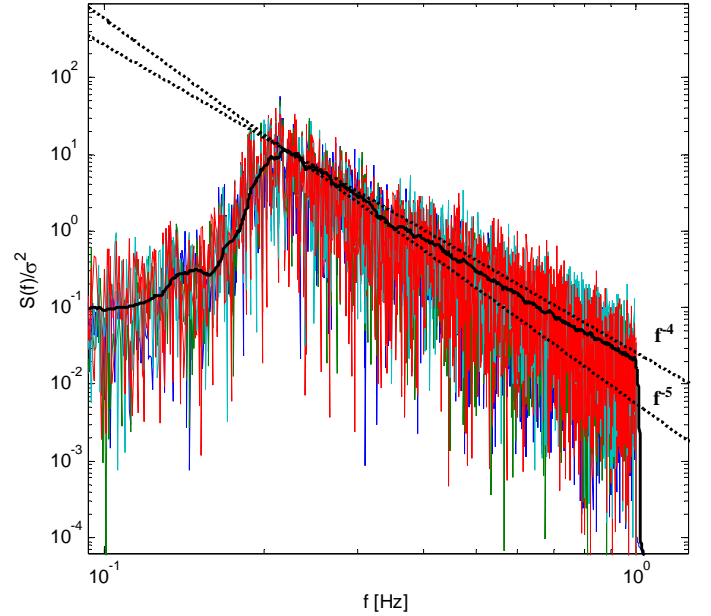

Figure 9. Experiment 2. Average frequency spectrum (black line) of the observed spectra (colored lines) at all the virtual probes indicated in Figure 8.
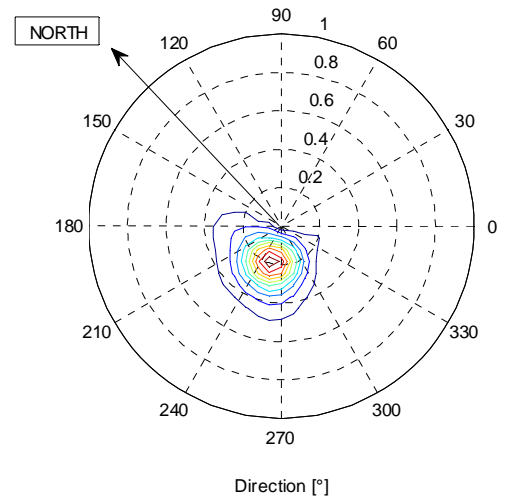

Figure 10. Experiment 2: Average wavenumber spectrum over 21000 3D reconstructed sea surface maps. Nyquist wavenumber: $[k_x, k_y]_{max}$ = [62.83 rad/m, 62.83 rad/m]. Spectral Resolution: dk_x=dk_y = 0.06 rad/m. North direction is rotated 46.2° (counterclockwise) with respect to the y-axis.
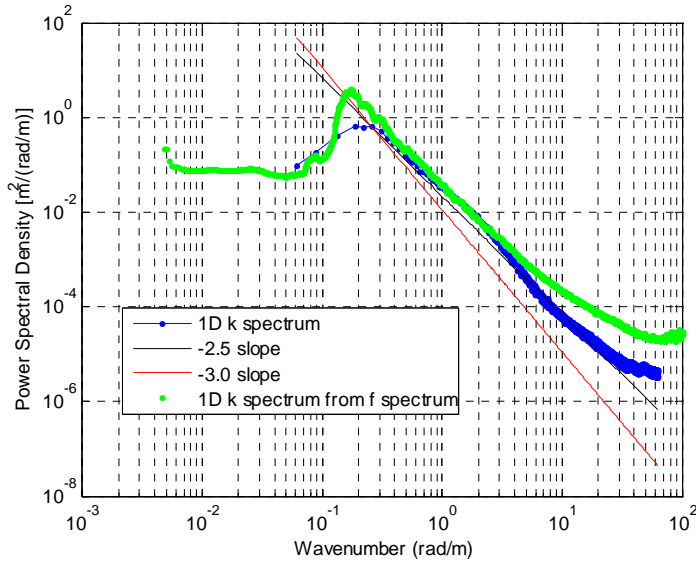
5   Copyright © 2011 by ASME

Figure 11. Experiment 2: Observed average omnidirectional spectrum S(k) (blue) and that obtained from the average frequency spectrum (green) via the linear relation.
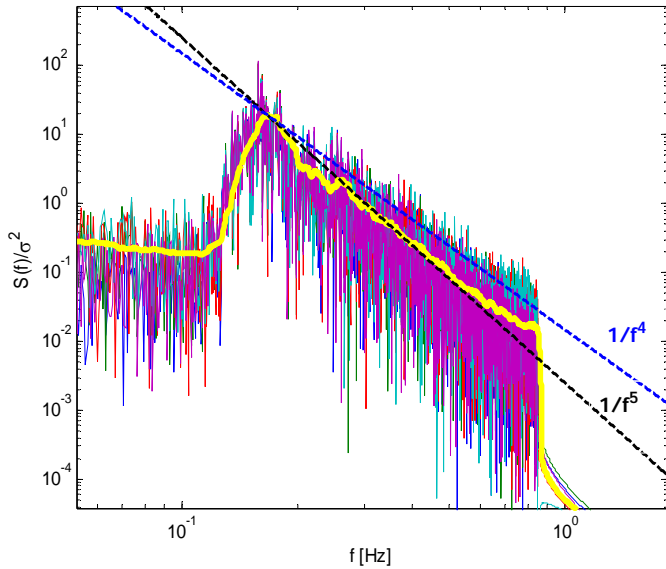

Figure 12. Experiment 3: Average frequency spectrum (yellow line) of the observed spectra (colored lines) at the virtual probes.
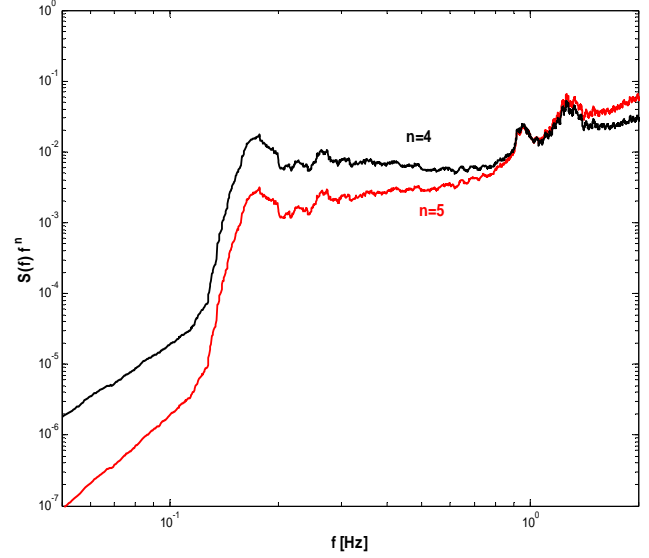

Figure 13. Experiment 3: Average saturation spectrum $S(f)f^n$ for n=4,5.

DOPPLER SHIFT DUE TO CURRENT

During Experiment 3, AWAC measured an underwater current that was mostly directed along the North direction and varied with depth as shown in Figure 15. In order to estimate the current from **WASS** measurements, we extract from the stereo-reconstructed wave space-time volume $\eta(x,y,t)$ the surface height $\eta(s,t)$ along the North direction s (see Figure 10) passing by the centre of the reconstructed domain. We then compute the 2D spectrum $S(k,f)$ of $\eta(s,t)$. On the domain (k,f) the amplitude map of S is given in Figure 14. The regions of non zero amplitudes identify the wave dispersion curve (black line). This does not match the theoretical dispersion curve (dot line)

$$k = \pm \frac{(2\pi f)^2}{g}, \tag{1}$$

possibly because (1) does not account for current effects underneath the wave surface. The Doppler-shift, which causes the mismatch between the observed dispersion and (1), allows estimating the current speed as follows. In presence of a current U_0 collinear with the direction of wave propagation, (1) becomes (Boccotti, 2000)

$$k = \pm \frac{(2\pi f - U_0 k)^2}{g}. \tag{2}$$

In reality U_0 in (2) is an average speed that accounts for the effects of long-wave modulation on short waves and the variability of current with depth. Since longer waves feel the current at the sea bottom whereas shorter waves that nearby the surface, U_0 is a function of k in the form

$$U_0(k) = 2k \int_{-\infty}^{0} U(z) \exp(2kz) \, dz , \qquad (3)$$

where $U(z)$ is the unknown current profile (Steward and Joy, 1974). As the current decays slower with depth, longer waves are affected by the deep current, whereas shorter waves are altered by the near-surface current. The best values for U_{max} and α If we assume an exponential profile such as

$$U(z) = U_{max} \exp(\alpha z), \qquad z \le 0, \qquad (4)$$

the average current in (2) follows from (3) as

$$U_0(k) = \frac{2kU_{max}}{2k + \alpha} . \qquad (5)$$

that match the observed dispersion curve with the theoretical form (2) are U_{max}=-0.45 m/s and $\alpha = 0.1$ 1/m, respectively. The fitted wave-current dispersion curve (2) is shown in Figures 14.
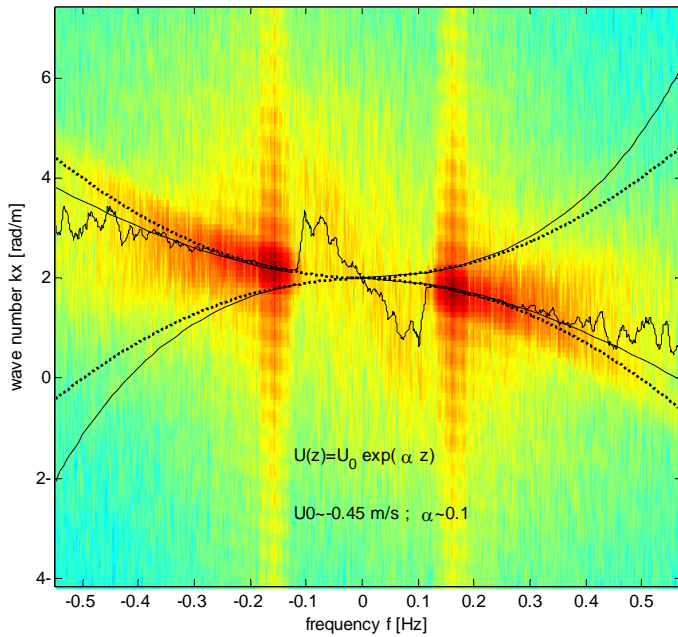

Figure 14. Experiment 3: 2D Log spectrum, observed dispersion curve (black line), theoretical dispersion curve without current (dot line) and with current (solid line).

WASS estimate of the current profile follows from (4) and it is shown in Figure 15 in comparison to that measured by the AWAC instrument operational at *Acqua Alta*. Finally, we note that the observed dispersion curve in Figure 14 shows a linear branch in the low-frequency range corresponding to a constant speed ~0.125 m/s. We speculate that this could be the wave-induced current generated by longer waves larger than the imaged area.
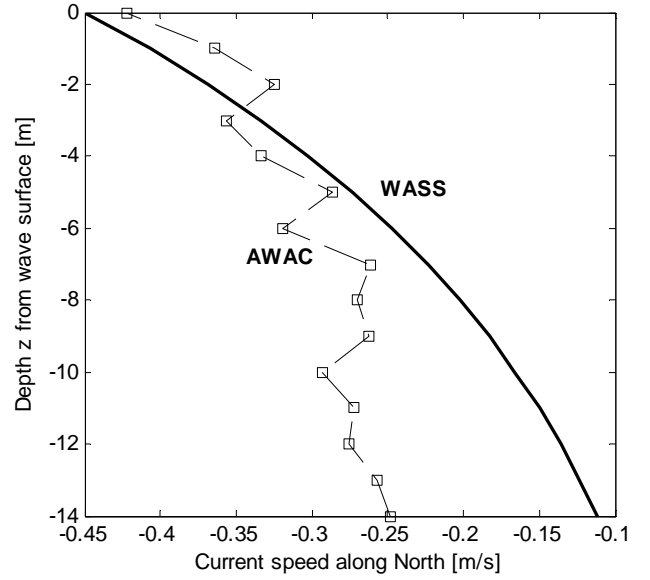

Figure 15. Experiment 3: AWAC current measurements and WASS estimates.

WAVE STATISTICS

By collecting the time waves observed at all the virtual probes indicated in Figure 8, we can now estimate the wave height distribution which is shown in Figure 16. It is observed a fair agreement with the Boccotti asymptotic form given by (Boccotti 2000, Tayfun and Fedele 2007)

$$P(H > h) = c \exp\left(-\frac{h^2}{4\sigma^2(1+\psi^*)}\right) \qquad (6)$$

Here, the parameter c depends upon ψ^*, the absolute value of the first minimum of the wave covariance (Boccotti, 2000).
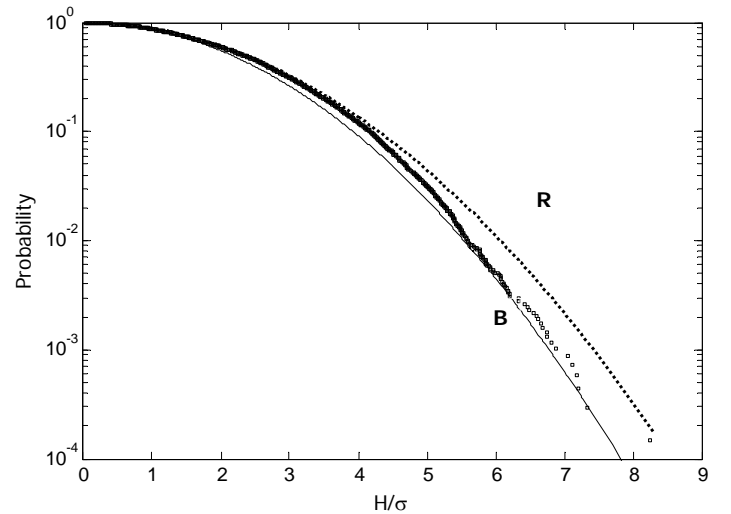

Figure 16. Experiment 2: Wave height exceedance probability; R=Rayleigh, B=Boccotti.

7   Copyright © 2011 by ASME

In particular, their mean values over the time series ensemble are $c \approx 1, \psi^* \approx 0.66$.

The observed crest/trough statistics is compared against the Tayfun-Fedele (TF) and Forristall (F) models in Figure 17. The TF distributions for crest (C) and trough (T) heights are given, respectively, by (Tayfun and Fedele 2007, Fedele 2008)

$$P(C > h) = \exp\left(-\frac{Z_c^2}{2}\right)\left(1 + \frac{\Lambda}{64}z^2(z^2 - 4)\right)$$

$$P(T > h) = \exp\left(-\frac{z^2}{2}(1 + 0.5\mu z)^2\right)\left(1 + \frac{\Lambda}{64}z^2(z^2 - 4)\right) \quad (7)$$

where $z = h/\sigma$, Z_c is derived from the quadratic equation $z = Z_c + \mu Z_c^2/2$, with μ as a characteristic parameter that measures wave steepness (Tayfun 1986, Fedele and Tayfun 2009) and Λ is a measure of quasi-resonant third order nonlinearities and it depends upon the fourth order cumulants of the wave surface η (Tayfun and Fedele 2007a). For our data set $\Lambda \cong 0$, and second order nonlinearities are dominant. The wave steepness can be estimated directly from data via time averages as $\mu = <\eta^3>$, where $<\bullet>$ denotes expectation. However, these estimators are usually statistically unstable. A stable estimate for μ can be defined from the moments of the wave spectrum as $\mu_a = \mu_m(1 - \nu + \nu^2)$ (Fedele and Tayfun 2009), where ν is the spectral bandwidth given by $\nu = \sqrt{m_0 m_2/m_1^2 - 1}$, where $m_j = \int f^j S(f) df$ are the spectral moments, and μ_m is the steepness for narrowband waves, i.e. as $\nu \to 0$, $\mu_m = \sigma \omega_m^2/g$, (Tayfun 1986) with $\omega_m = m_1/m_0$ as the mean up-crossing frequency. The observed values for these parameters are given by $\mu = 0.080$, $\mu_m = 0.090$, $\mu_a = 0.069$ and $\nu = 0.52$. The Forristall (2000) model for crest heights is expressed as

$$P(C > z) = \exp\left[-\left(\frac{z}{4\alpha}\right)^\beta\right]. \quad (8)$$

Here, the parameters α and β depend upon the sea directionality and

$$S_1 = \frac{2\pi}{g}\frac{H_s}{T_m^2}, \qquad U_r = \frac{H_s}{k_m^2 d^3}. \quad (9)$$

The observed values are: $S_1 \approx 0.071$, $U_r \approx 0$, and for unidirectional (2D) and multidirectional (3D) seas $\alpha_2 = 0.374$, $\beta_2 = 1.848$ and $\alpha_3 = 0.372$, $\beta_3 = 1.874$, respectively. The observed crest exceedance in Figure 17 agrees well with both the TF and F models (see Eqs. 7 and 8 respectively). Further, the observed trough statistics is in good agreement with the TF model (7) as well.
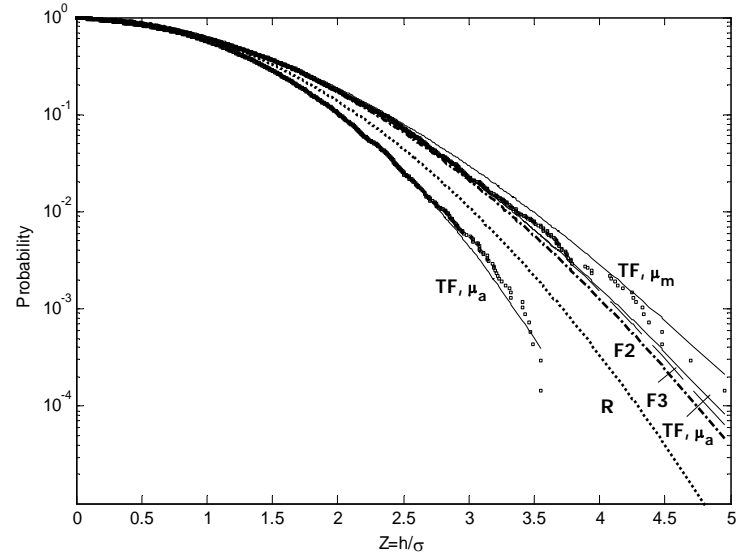

Figure 17. Experiment 2: Wave crest exceedance probability; R=Rayleigh, TF=Tayfun-Fedele model with steepness μ , F2=2D Forristall, F3=3D Forristall.

GUMBEL EXTREMES

For one dimensional data, i.e. time series, the expected maximum wave height $Z(N) = <H_{max}/\sigma>$ of N observed waves according to a Gumbel statistics is given by (Tayfun and Fedele 2007)

$$Z(N) = \sqrt{\log(c_0 N)/c_1} + \frac{\gamma_e}{2\sqrt{c_1 \log(c_0 N)}}, \quad (10)$$

where $\gamma_e \approx 0.5772$, and $c_0 = 1$, $c_1 = 1/8$ for the Rayleigh model, and

$$c_0 = (1 + b)/\sqrt{2b(1-a)}, c_1 = 0.25/(1-a) \quad (11)$$

for the Boccotti model with $a = -\psi^*, b \approx 1$. Both the Rayleigh (R) and Boccotti (B) models are compared against data in Figure 18. R overestimates the observed expected maximum wave heights as expected because it does not account for bandwidth effects as B does.

Further, the expected maximum crest height $C_T(N) = <C_{max}/\sigma>$ of N observed waves in one dimensional data is given by (Tayfun and Fedele 2007)

$$C_T(N) = h_N + \frac{\mu}{2}h_N^2 + \gamma_e\left(\mu + \frac{1}{h_N}\right), \quad (12)$$

where $h_N = \sqrt{2\log N}$. Since we have gathered together waves of time series observed at different points (virtual probes shown in Figure 8) over an area, the observed extremes could

be larger than those from a time series extracted at only one point in space. Indeed, if we gather together time series from P point-probes, and for each of them we observe N waves, then from (12) it follows that $C_T(N) < C_T(NP)$. This is correct as long as waves are short-crested and probes are well separated in space to assure the stochastic independence among measurements at different points in space.
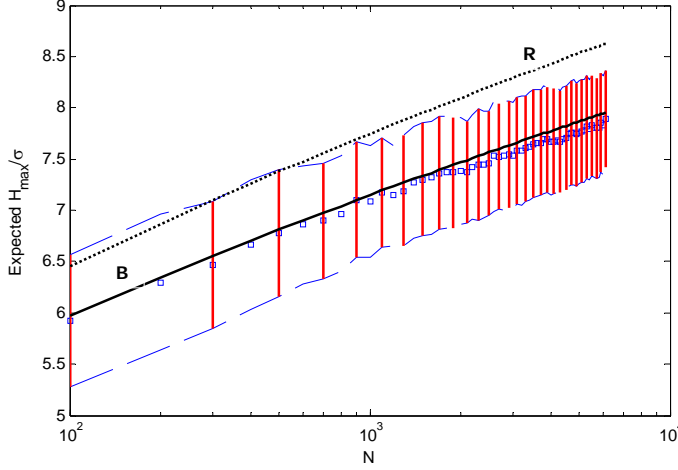

Figure 18. Experiment 2: Expected maximum crest height: observed average max wave height amplitudes (square dots) and relative stability bands $Z(N) \pm \sigma_N$, σ_N being the associated standard deviation, and theoretical R=Rayleigh, B=Boccotti models, respectively.

To account for spatial effects in our extreme value analysis, we consider as a reference statistics that of the expected maximum crest height $C_\beta(N)$ of N waves whose parent statistical distribution follows the general law

$$P(h > z) = z_1^\beta \exp(-z_1^2 / 2), \qquad \beta \geq 1, \qquad (13)$$

where the linear amplitude z_1 satisfies the Tayfun quadratic equation $z = z_1 + \mu z_1^2 / 2$ (Tayfun 1986) to account for second order nonlinearities. In this case, the expected maximum crest height depends upon the parameter β and it is given by

$$C_\beta(N) = h_N + \frac{\mu}{2} h_N^2 + \gamma_e \frac{1 + \mu h_N}{h_N - \beta / h_N}, \qquad (14)$$

where h_N satisfies $h_N^\beta \exp(-h_N^2/2) = 1/N$. For $\beta = 0$ the Tayfun model is recovered, as it should be. The 2D and 3D Tayfun-Piterbarg models are obtained for β equal to 1 and 2, respectively. The theoretical model (14) is compared against the observed crest heights as shown in Figure 19. The associated expected maximum crest height does not deviate from the 1D statistics based on the Tayfun model. This may occurs because the P largest crests observed at the virtual

probes do not occur simultaneously in time since the probe grid is sparse.

In the following we will investigate the extreme value statistics of the largest amplitude of the wave surface η over a given area A. To do so, consider the sequence $\{\xi_1, \xi_2, \ldots, \xi_N\}$ of the instantaneous maximum $\xi(t) = \eta_{\max}(t) / \sigma$ of η over the imaged area, sampled at 5 Hz. The expected maximum $\xi_{\max}(N)$ is computed according to the Gumbel statistics $C_\beta(N)$ of (14) and compared it against the observed expected maximum amplitude in Figure 20. As the area increases, the observations deviate from the 1D Tayfun model approaching the 2D Tayfun-Piterbarg statistics.
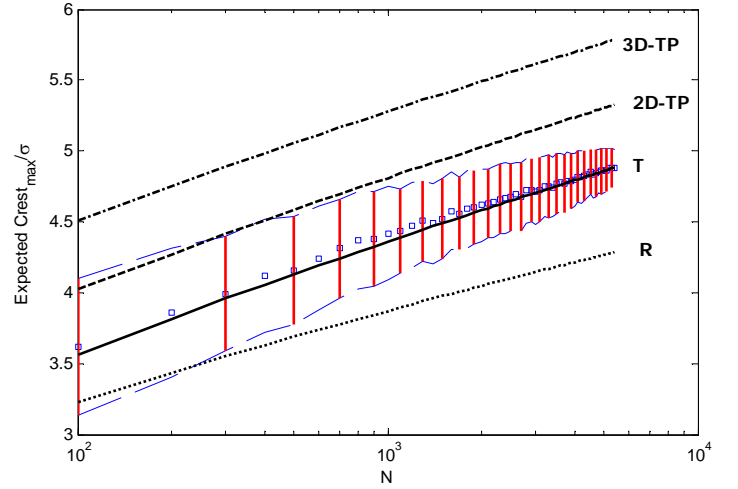

Figure 19. Experiment 2: Expected maximum crest height: observed average max crest amplitudes (square dots) and relative stability bands $C(N) \pm \sigma_N$, σ_N being the associated standard deviation, and theoretical R=Rayleigh, T=Tayfun, TP= Tayfun-Piterbarg models.
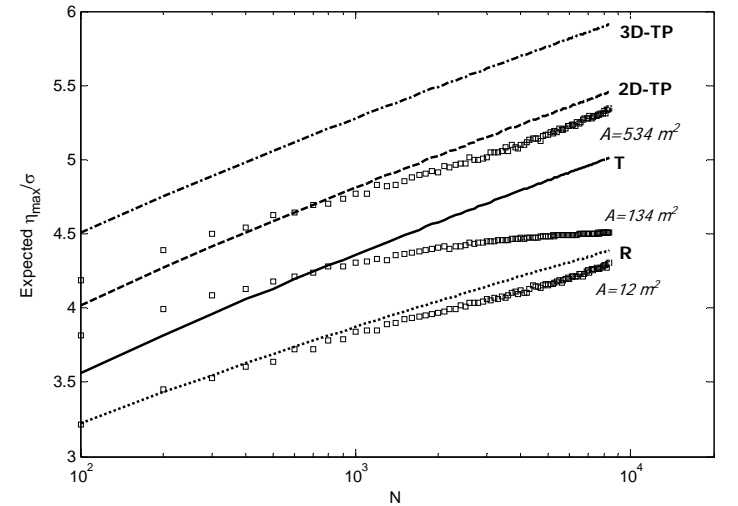

Figure 20. Experiment 2: Expected maximum of the wave surface as function of the area A against theoretical models.

Copyright © 2011 by ASME

The crest-to-trough height H of the largest waves observed at the various different virtual probes do not violate the *Miche-Stokes upper bound* (see Figure 21)

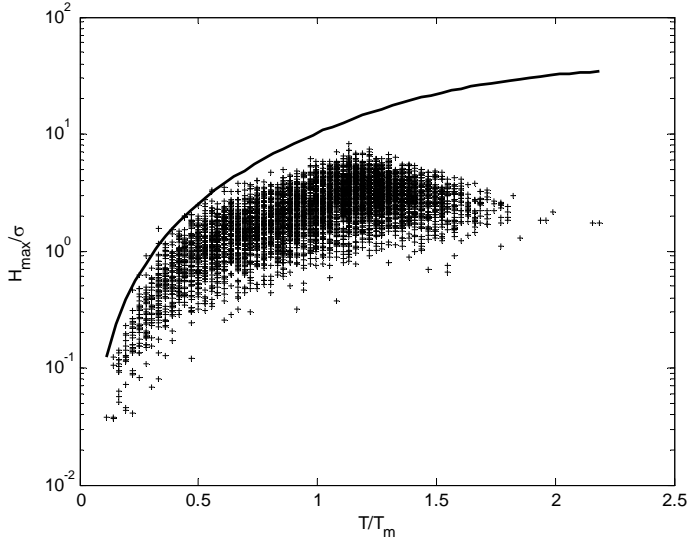$$\frac{H}{\sigma} \leq \frac{2\pi}{7} \frac{\tanh(kd)}{k\sigma}. \tag{15}$$

Figure 21. Experiment 2: Theoretical Miche-Stokes upper bound for the crest-to-trough height H (black line) and observed pairs $(T/T_m, H/\sigma)$ (red dots), with σ and T_m as the wave surface standard deviation and mean wave period, respectively.

EXPECTED SHAPE OF LARGE WAVES

Consider among the observed waves, those with large crest-to-trough amplitudes $\alpha = H/\sigma \gg 1$. The shape of these large waves tends, for $\alpha \gg 1$, to the deterministic form

$$< \eta(t) | \alpha > = \frac{\alpha}{2} \frac{\psi(t) - \psi(t - T^*)}{1 - \psi(T^*)} +$$
$$+ \frac{\mu \alpha^2}{8} \left\{ \left[\frac{\psi(t) - \psi(t - T^*)}{1 - \psi(T^*)} \right]^2 - \left[\frac{\hat{\psi}(t) - \hat{\psi}(t - T^*)}{1 - \psi(T^*)} \right]^2 \right\}, \tag{16}$$

where $\psi(t)$ is the normalized wave covariance, $\hat{\psi}(t)$ its Hilbert transform, and T^* is the abscissa of the first absolute minimum of ψ (Boccotti 2000). Further, if we define C and T as the crest and trough amplitudes of the same wave, given $\alpha \gg 1$, the conditional ratio C/T is given by

$$\{C/T | H = \alpha\} = \frac{1 + 2\gamma Z}{1 - 2\gamma Z} \cdot \frac{1 + \mu\alpha(1 + 2\gamma Z)/4}{1 - \mu\alpha(1 - 2\gamma Z)/4}, \tag{17}$$

where Z is Gaussian with mean zero and unit variance and

$$\gamma = \frac{1}{\alpha} \sqrt{\frac{1 + \psi(T^*)}{2}}. \tag{18}$$

Figure 22 shows a fair agreement between the observed shape of large waves and the theoretical expected form (16) ($\mu = \mu_m = 0.09$ and $\psi(T^*) = -0.66$). Further, Figure 23 shows that the observed conditional ratio agrees well with the associated theoretical expected value from (17).
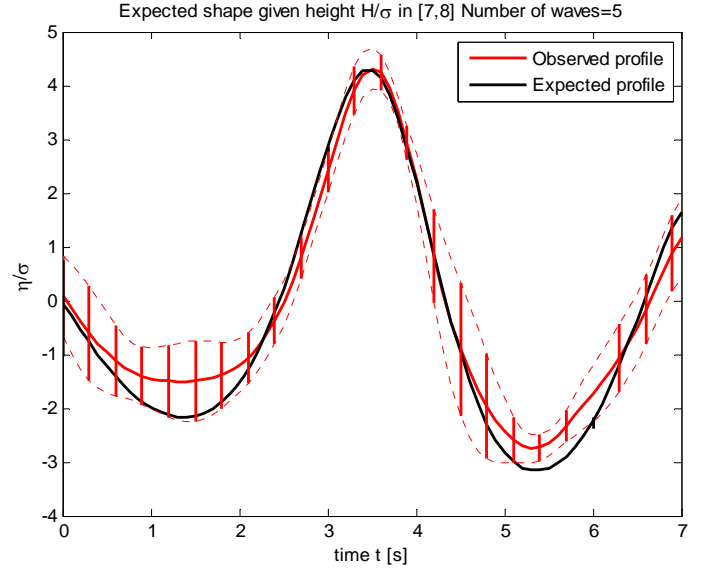

Figure 22. Experiment 2: Observed shape of large waves (red line) given the crest-to-trough height H in $[7\sigma, 8\sigma]$ and respective stability bands, and theoretical expected wave profile of Eq. 16 (black line).
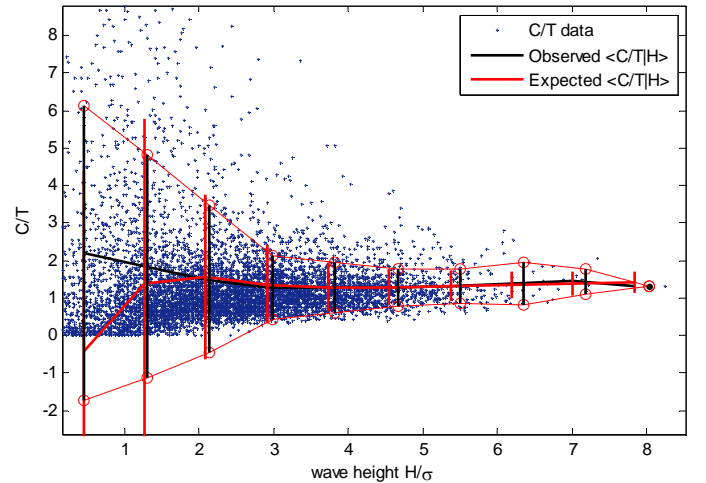

Figure 23. Experiment 2: Observed crest-to-trough ratio (red line) given the crest-to-trough height H and respective stability bands, and the theoretical expected conditional ratio of Eq. 17 (black line).

10   Copyright © 2011 by ASME

Consider now among the observed waves, those with large crest amplitudes $\xi = h/\sigma \gg 1$. Their shape tends to

$$< \eta(t) | \eta(0) = \xi > = \xi_1 \psi(t) + \frac{\mu \xi_1^2}{2}[\psi^2(t) - \hat{\psi}^2(t)],$$

where $\xi = \xi_1 + \mu \xi_1^2 / 2$ (Lindgren 1970,1972; Boccotti, 2000, Tayfun and Fedele 2007, Fedele and Tayfun 2009). Figure 24 shows a comparison between the observed shape of waves with large crests and the respective theoretical expected wave profiles. The agreement with theory is good.
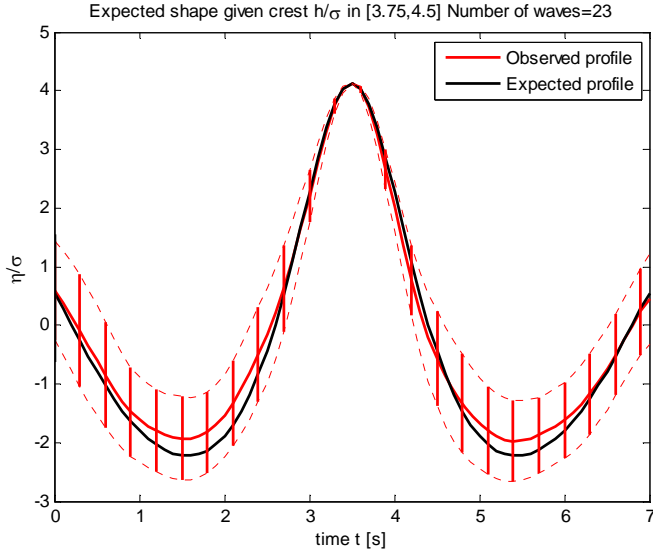

Figure 24. Experiment 2: Observed shape of large waves (red line) given the crest amplitude h in [3.75σ, 4.5σ] and respective stability bands, and theoretical expected wave profile (black line).
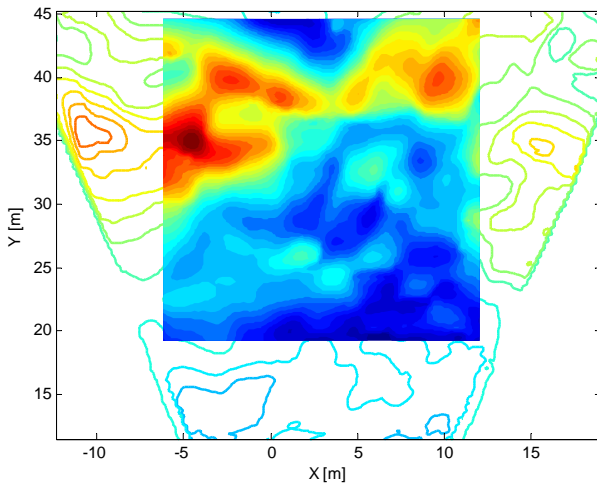

Figure 25. Experiment 3: selected region S.

SPATIAL ANALYSIS VIA EULER CHARACTERISTICS

Consider a 2D snapshot $\eta(x, y)$ of the wave surface at a given time t over a given rectangular region S of dimensions l_x and l_y as that shown in Figure 25 from Experiment 3. The excursion set $U_{\eta,h} = \{(x, y) \in S : \eta(x, y) > h\}$ is the portion of S over which η is above the threshold h. For this set, the Euler characteristic EC is defined as the difference between the number of connected components and holes of the given set. If the threshold is low, then EC counts the number of holes in the given set. If the threshold is high, then all the holes tend to disappear and the EC counts the number of connected components, or local maxima of the wave surface. For weakly nonlinear wave surfaces, the expected value of the EC is given by (Adler 1981, Worsley 1995, Adler and Taylor 2007)

$$< EC(\xi) > = EC_a(\xi_1) + EC_b(\xi_1) + \Pr[Z > \xi_1] \quad (19)$$

where

$$EC_{area} = N_S \, \xi_1 \exp(-\xi_1^2 / 2), \quad EC_b = N_P \exp(-\xi_1^2 / 2). \quad (20)$$

Here, $< \bullet >$ denotes expectation, $\xi = h/\sigma$ is a normalized threshold amplitude which satisfies $\xi = \xi_1 + \mu/2 \, \xi_1^2$, and Z is Gaussian with zero mean and unit variance. Further,

$$N_S = \sqrt{2\pi} \, \frac{l_x l_y}{\overline{L}_x \overline{L}_y} \sqrt{1 - \alpha_{xy}^2}, \quad N_P = \frac{l_x}{\overline{L}_x} + \frac{l_y}{\overline{L}_y}. \quad (21)$$

are the average number of 'waves' over the area A_S and along the perimeter P, respectively, and $\overline{L}_x$ and $\overline{L}_y$ are the mean wavelength along two orthogonal directions x and y, respectively. Note that the wave parameters in (21) can be expressed solely in terms of the moments of the directional spectrum (Baxevani and Richlik 2004).

The EC_b term in (19) will be referred to as a boundary correction because it is important when the excursion set touches the boundary/perimeter of the region S (Worsley 1995). Adler (1981) and Adler and Taylor (2007) have shown that the probability that the global maximum of a random field η exceeds a threshold h is well approximated by the expected EC of the excursion set $U_{\eta,h}$, provided the threshold is high. Indeed, as the threshold h increases, the holes in the excursion set disappear until each of its connected components includes just one local maximum, and the EC counts the number of local maxima. For very large thresholds, the EC equals 1 if the global maximum exceeds the threshold and 0 if it is below. Thus, heuristically the $EC(U_{\eta,h})$ of large excursion sets is a binary random variable with states 0 and 1, from which follows that the probability of exceedance of the global maximum $\eta_{max} = \max(\eta)/\sigma$ of η over S is given, for $h \gg \sigma$, by

$$\Pr(\eta_{max} > \xi) = \Pr[EC(U_{\eta,h}) = 1] = < EC(\xi) > . \quad (22)$$

Further, the expected value of η_{max} stems from a Gumbel asymptotics as

$$<\eta_{max}> = h_N + \frac{\mu}{2}h_N^2 + \gamma \frac{1+\mu h_N}{h_N - \dfrac{N_S}{N_S h_N + N_P}} , \qquad (23)$$

where h_N satisfies $(N_S h_N + N_P)\exp(-h_N^2/2) = 1$. If $N_P = 0$, the Tayfun-Piterbarg model is recovered (Krogstad et al. 2004).

Figure 26 reports the time variation of the estimated expected maximum $<\eta_{max}>$ computed both with and without boundary corrections ($N_P = 0$). For comparison, we also plotted the observed maximum height over S and the maximum height expected along its boundary P. Further, we computed the EC for each of η-snapshot (9000 in total), the associated expected EC value and standard deviation, respectively.
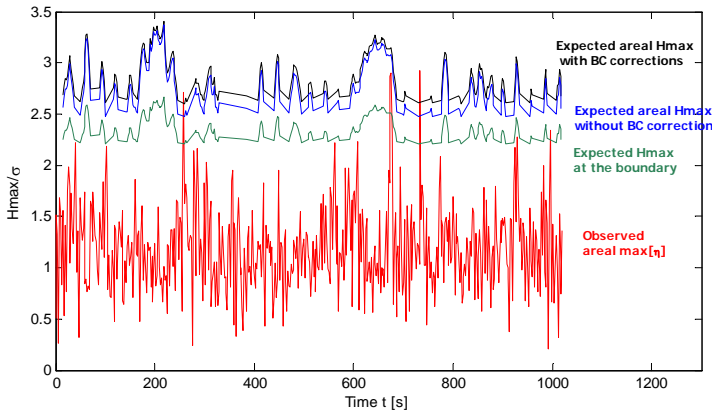

Figure 26. Experiment 3: Time variation of the expected maximum wave surface over the large area S of Figure 25 computed with and without boundary corrections (black and blue lines, respectively), the expected maximum along the boundary of S (green line) and the observed maximum over the area from data (red line).
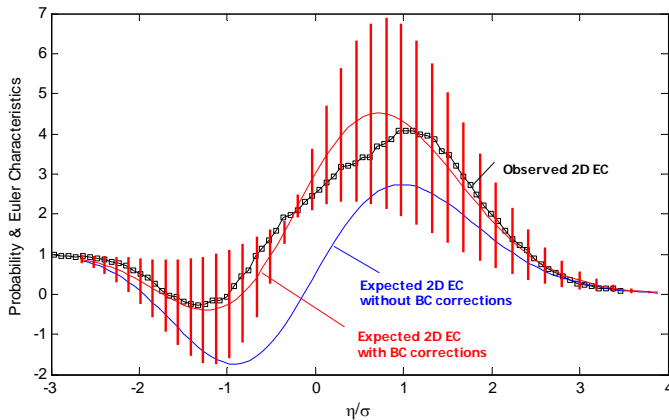

Figure 27. Experiment 3: observed Euler Characteristics and theoretical expected values over the area S of Figure 25.
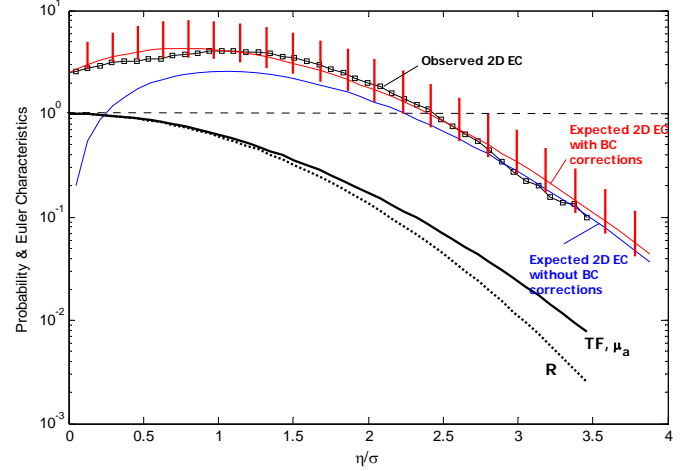

Figure 28. Experiment 3: Observed Euler Characteristics and theoretical expected values compared to the R=Rayleigh and TF=Tayfun-Fedele models, respectively.

Figure 27 shows the observed average EC and the respective stability bands. Good agreement with their theoretical expectations is found when the boundary corrections EC_b are accounted for. Further, from Figure 28 it is also clear that the asymptotic EC-based exceedance probability of the wave surface maximum (valid for $\eta > 2.5\sigma$) deviates from both the Rayleigh and Tayfun-Fedele models. This provides evidence that the expected maximum surface height estimated over the imaged area is considerably larger than the expected maximum crest at a single point in space.

CONCLUSIONS

We have deployed a novel Wave Acquisition Stereo System (**WASS**) at the oceanographic tower *Acqua Alta* off the Italian Venice coast. As a video observational technology, **WASS** was able to provide a multi-dimensional image of the oceanic state around the tower under both Bora and Scirocco wave conditions. To do so, advanced stereo techniques based on the epipolar geometry were exploited to obtain 3D reconstructions of the sea surface map in time. By just exploiting time series of reconstructed wave surface displacements extracted at virtual point probes, we proved that the accuracy of the **WASS** measurements is comparable to that of more traditional wave instruments. Further, the statistics of crest and trough heights, as well as that of crest-to-trough heights estimated via **WASS** agree very well with well known theoretical models, such as the Forristall and Tayfun-Fedele distributions for crests and the Boccotti model for wave heights. We also proposed novel techniques for estimating wave spectra, dispersion and currents from the stereo-reconstructed wave surface. Finally, a statistical analysis of the reconstructed spatial snapshots based on Adler's Euler Characteristics revealed that the expected maximum wave surface height over an area is larger than that expected at a given point in space.

REFERENCES

Adler, R.J., 1981. *The Geometry of Random Fields*, New York: John Wiley.

Adler, R.J. & Taylor, J.E., 2007. *Random fields and geometry*. Springer Monographs in Mathematics Springer, New York.

Banner, M. L., Jones, S. F., Trinder, J. C., 1989. Wavenumber spectra of short gravity waves. *Journal of Fluid Mechanics*, 198: 321-344.

Baxevani, A., and I. Richlik, 2004. Maxima for Gaussian seas. *Ocean Engn.,* 33(7), 895-911.

Benetazzo, A., 2006. Measurements of short water waves using stereo matched image sequences Coastal Engineering 53:1013-1032

Boccotti P., 2000. *Wave Mechanics for Ocean Engineering*. Elsevier Science, Oxford.

Fedele, F. 2008. Rogue Waves in Oceanic Turbulence. *Physica D* 237, 14-17:2127-2131

Fedele F. and Tayfun, M.A. 2009. On nonlinear wave groups and crest statistics" *J. Fluid Mech.* 620, 221-239

Forristall, G. Z., 2000. Wave crests distributions: observations and second order theory. *J. Phys. Oceanogr.*, 38(8): 1931–1943.

Forristall, G.Z. 2006, Maximum wave heights over an area and the air gap problem, OMAE2006-92022 paper, *Proc. ASME 25th Inter. Conf. Off. Mech. Arc. Eng.*, Hamburg.

Forristall, G.Z. 2007, Wave crest heights and deck damage in Hurricanes Ivan, Katrina and Rita, Offshore Technology Conference Proceedings, OTC 18620, Houston.

Holland, K.T. and R.A. Holman. 1997. Video estimation of foreshore topography using trinocular stereo. *Journal of Coastal Research* 13(1): 81-87

Holland, K.T., R.A. Holman, T.C. Lippmann, J. Stanley, and N. Plant. 1997. Practical use of video imagery in nearshore oceanographic field studies. *IEEE Journal of Oceanic Engineering* 22(1): 81-92..

Krogstad, H.E., Liu, J., Socquet-Juglard H., Dysthe K.B. and K. Trulsen, 2004 Spatial Extreme Value Analysis of Nonlinear Simulations of Random Surface Waves, OMAE2004-51336 paper, *Proc. ASME 23th Inter. Conf. Off. Mech. Arc. Eng.*, Vancouver.

Lindgren, G. 1970. Some properties of a normal process near a local maximum. *Ann. Math. Statist.* 4(6),1870-1883.

Ma, Y. Soatto, S., Kosecka, J., Shankar Sastry, S., 2004. *An invitation to 3-D vision: from \images to geometric models.* Springer-Verlag New York

Phillips, O.M., 1958. The equilibrium range in the spectrum of wind-generated waves, *Journal of Fluid Mechanics*, vol. 4, no. 4, pp. 426-434.

Piterbarg V. 1995 *Asymptotic Methods in the Theory of Gaussian Processes.* American Mathematical Society, ser. Translations of Mathematical Monographs, Vol. 148, 205pp.

Santel, F., Heipke, C., Könnecke, S., Wegmann, H., 2002. Image Sequence Matching for the Determination of three-dimensional Wave Surfaces. P*roceedings of the ISPRS Commission V Symposium*, Corfu, Greece, Volume XXXIV Part 5, 596-600.

Shemdin, O. H., Tran, H. M., Wu, S. C., 1988. Directional Mesurements of short ocean waves with stereography. *Journal of Geophysical Research*, 93, 13891-13901.

Stewart RH, Joy JW. 1974 HF radio measurements of surface currents. Deep-sea research **21**(12):1039-1049

Tayfun, MA 1986. On narrow-band representation of ocean waves. Part I: Theory. *J. Geophys. Res.*, (1(C6):7743-7752

Tayfun, M.A., Fedele, F., 2007, Wave-height distributions and nonlinear effects, *Ocean Engineering*, vol. 34, no. 11-12, pp. 1631-1649

Wanek, J.M. and Wu, C.H., 2006. Automated trinocular stereo imaging system for three-dimensional surface wave measurements, *Ocean Engineering*, 33(5-6) 723-747.

Worsley, K.J. 1995. Boundary corrections for the expected Euler characteristic of excursion sets of random fields, with an application to astrophysics. *Adv. App. Prob.*, 27:943-959.

Zakharov, V.E., 1999, Statistical theory of gravity and capillary waves on the surface of a finite-depth fluid, *Eur. J. Mech. B Fluids* 18(3):327-344